How to cite: *Angew. Chem. Int. Ed.* **2023**, *62*, e202306585
doi.org/10.1002/anie.202306585

Upconversion Nanophosphors

Cross Relaxation Channel Tailored Temperature Response in Er^{3+}-rich Upconversion Nanophosphor

Kefan Wu, Enhui Wang, Jun Yuan, Jing Zuo, Ding Zhou, Haifeng Zhao, Yongshi Luo, Ligong Zhang, Bin Li, Jiahua Zhang, Langping Tu, and Hong Zhang**

Abstract: Recently high doping of lanthanide ions (till 100 %) is realized unprecedentedly in nanostructured upconversion (UC) phosphors. However, oddly enough, this significant breakthrough did not result in a corresponding UC enhancement at ambient temperature, which hinders the otherwise very interesting applications of these materials in various fields. In this work, taking the Er^{3+}-rich UC nanosystem as an example, we confirm unambiguously that the phonon-assisted cross relaxation (CR) is the culprit. More importantly, combining the theoretical modeling and experiments, the precise roles of different CR channels on UC energy loss are quantitatively revealed. As a result, lowering the temperature can exponentially enhance the relevant UC luminescence by more than two orders of magnitude. Our comprehension will play an important role in promoting the UC performance and further application of high doping rare earth materials. As a proof of concept, an Er^{3+}-rich core/multi-shell nanophosphor is exploited which demonstrates the great potential of our finding in the field of ultra-sensitive temperature sensing.

[*] K. Wu, Prof. H. Zhao, Prof. Y. Luo, Prof. L. Zhang, Prof. B. Li, Prof. J. Zhang, Dr. L. Tu
State Key Laboratory of Luminescence and Applications, Changchun Institute of Optics, Fine Mechanics and Physics, Chinese Academy of Sciences
130033 Changchun, Jilin (China)
E-mail: tulangping@163.com

K. Wu, J. Yuan, Prof. H. Zhang
Van't Hoff Institute for Molecular Sciences, University of Amsterdam
Science Park 904, 1098 XH Amsterdam (The Netherlands)
E-mail: h.zhang@uva.nl

E. Wang, Dr. J. Zuo
Key Laboratory of Automobile Materials (Ministry of Education), College of Materials Science and Engineering, Jilin University
130025 Changchun, Jilin (China)

Prof. D. Zhou
Hospital of Stomatology, Jilin University
130021 Changchun, Jilin (China)

Introduction

Trivalent lanthanide ions doped upconversion nanoparticles (UCNPs) are regarded as one of the most efficient non-linear luminescence materials, and their efficiency is orders of magnitude higher at low excitation power densities than other typical non-linear luminescence techniques, such as second harmonic generation.[1] UCNPs also possess high photostability and low biological toxicity. In the past two decades, UCNPs have attracted numerous research interests for application in, but not limited to, bio-imaging and photo-induced therapy,[2] anti-counterfeiting,[3] super-resolution spectroscopy,[4] and multicolor display.[5]

Conventional UCNPs are primarily based on sensitizer-activator co-doping strategy (e.g., Yb^{3+}/Nd^{3+} co-doped with Er^{3+}/Tm^{3+}/Ho^{3+}).[6] According to the knowledge obtained from their bulk counterparts, the concentrations of dopants must be kept at very low levels due to the known "concentration quenching" effect.[7] Recent advances in synthetic chemistry have enabled the significant progress of precisely tailored nanostructures, which has naturally triggered the exploration of the nano-size effect on dopant concentration restriction.[8] An impressive breakthrough has been realized since 2017, e.g., upconversion (UC) luminescence of Er^{3+} singly doped core–shell UCNPs do not saturate even with Er^{3+} concentration up to 100 %, while based on the traditional concept, this value should be less than 5 %.[9] The impressive promotion is ascribed to the passivation effect of inert shell, which cuts off the negative influence of surface-related quenching sites on Er^{3+}. The exploitation of Er^{3+}-rich core–shell structure not only breaks through the limitation of the alternative excitation wavelength of UC materials, such as Yb's 980 nm, so that 800, 980 and 1530 nm can be experimentally up-converted to shorter wavelengths through Er^{3+}-Er^{3+} self-sensitization,[10] but also induces strong signal of MRI/CT measurements,[11] which benefits greatly the applications in solar energy exploitation, multi-modal synergistic UC imaging, and photodynamic therapy, immunotherapy, et al.[12]

Despite these exciting progresses, the UC efficiency of Er^{3+}-rich core–shell structure at ambient temperature is still not satisfactory from the application point of view. Intensified ion-ion detrimental interaction brought by high dopant concentration strongly offsets the benefit of the significant increase in the number of activators. How to reduce the energy loss caused by the interaction has thus become an urgent problem. Most recently, an impressive progress has been achieved by our group, i.e., via introducing a cryogenic

field (e.g., 40 K), we found the UC luminescence of Er^{3+}-rich core–shell nanosystems (represented by $NaErF_4@NaYF_4$) can be tremendously boosted over 100-folds.[13] However, the relevant working mechanism remains vague. Specifically, despite the cross relaxation (CR) inhibition in low temperature is determined to be the leading cause of the UC enhancement, the accurate quantitative correlation between UC intensity and the environment temperature is still absent, which is actually the basis of all relevant investigations and applications in the future. This demand is particularly urgent when we take the complex interactions among multi-energy levels and multi-ions of Er^{3+}-rich UC system into consideration. As shown in Figure 1, numerous CR channels are possibly involved in this multi-ion system. Furthermore, the contributions of these channels to UC are also manipulated by diverse environmental conditions, such as temperature and excitation power density (Figure 1c), which makes the quantitative analysis more challenging.

Herein, combining the theoretical and experimental results, for the first time, we unveil the exponential relation between the green UC intensity of Er^{3+}-rich nanosystems and the environment temperature. From our results, the observed super-temperature-sensitivity of the green UC luminescence is actually the joint effects of two types of phonon-assisted Er-Er CR processes, whose contributions rely on, and thus can be quantitatively modulated by, excitation power density. Furthermore, based on this new discovery, we have designed an Er@Y@YbTm@Y (i.e., $NaYF_4$:75 %Er^{3+}@$NaYF_4$@$NaYF_4$:75 %Yb^{3+}, 2 %Tm^{3+}@$NaYF_4$) multi-layers temperature nano-sensor, of which the absolute and relative temperature sensitivities are over 10-fold higher than traditional Yb^{3+}/Er^{3+} co-doped counterparts below 150 K. These results have not only clarified the microscopic physical image of multiple CR processes in Er^{3+}-rich UC phosphors, but also demonstrated the possibilities of noble functions, which shall greatly promote the exploration and application of newly appeared highly doped rare earth luminescent nanomaterials.

Results and Discussion

In order to display the high temperature sensitivity of the photoluminescence (PL) of Er^{3+}-rich nanostructures and to determine the optimized doping concentration of Er^{3+}, a series of high-quality UCNPs are synthesized, i.e., $NaYF_4$:x %Er^{3+}@$NaYF_4$ (xEr@Y for short, x = 25, 50, 75, 100, respectively). The microscope images and XRD results are displayed in Figure 2a, b and Figure S1–3 which show pure hexagonal-phase nanoparticles with uniform size and morphology (i.e., 18.7 nm core with 6.2 nm shell). As the Er^{3+} concentration in the core increases, the effects of intensified Er-Er CR (negative factor) and increased activators (positive factor) will compete for the UC intensity. Interestingly, for these high-level-doping systems (Er^{3+} varies from 25 % to 100 %), significant enhancement is ubiquitously observed when the temperature goes down. The overall UC luminescence intensities (integrate from 500 to 700 nm) increase within the range of 13–22.5 times when the temperature drops down to 80 K (Figure 2c, d, under the 10 W/cm^2 980 nm excitation, detailed UC spectra are shown in Figure S4–6), which well agrees with our previous report.[13] Looking closely, it could find that the temperature response is emission wavelength dependent and the green light is obviously more sensitive than the red one (e.g., enhancing 193 folds vs 12 folds for 75Er@Y structure), which can be reasonably attributed to the consequence of phonon-assisted CR involved green→red emission transfer (Figure 2e). Specifically, red emission can be partly compensated by the green→red Er-Er CR, which lifts the red/green emission ratio at relatively high temperatures.[13,14] Therefore, in the following work, only the green UC emission (rather than red emission or the overall UC intensity) is selected as the response signal for temperature detection.

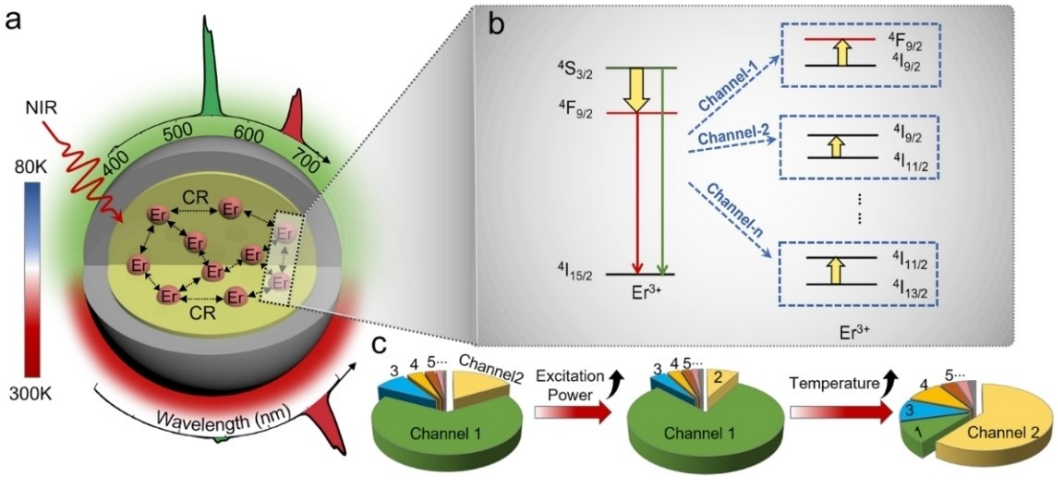

Figure 1. a) Schematic diagram of the temperature related UC process in Er^{3+}-rich core–shell nanosystem. b) Numerous potential different phonon-assisted CR channels in Er^{3+}-rich nanosystem. c) Temperature and excitation-power-density controlled proportional of different CR channels.

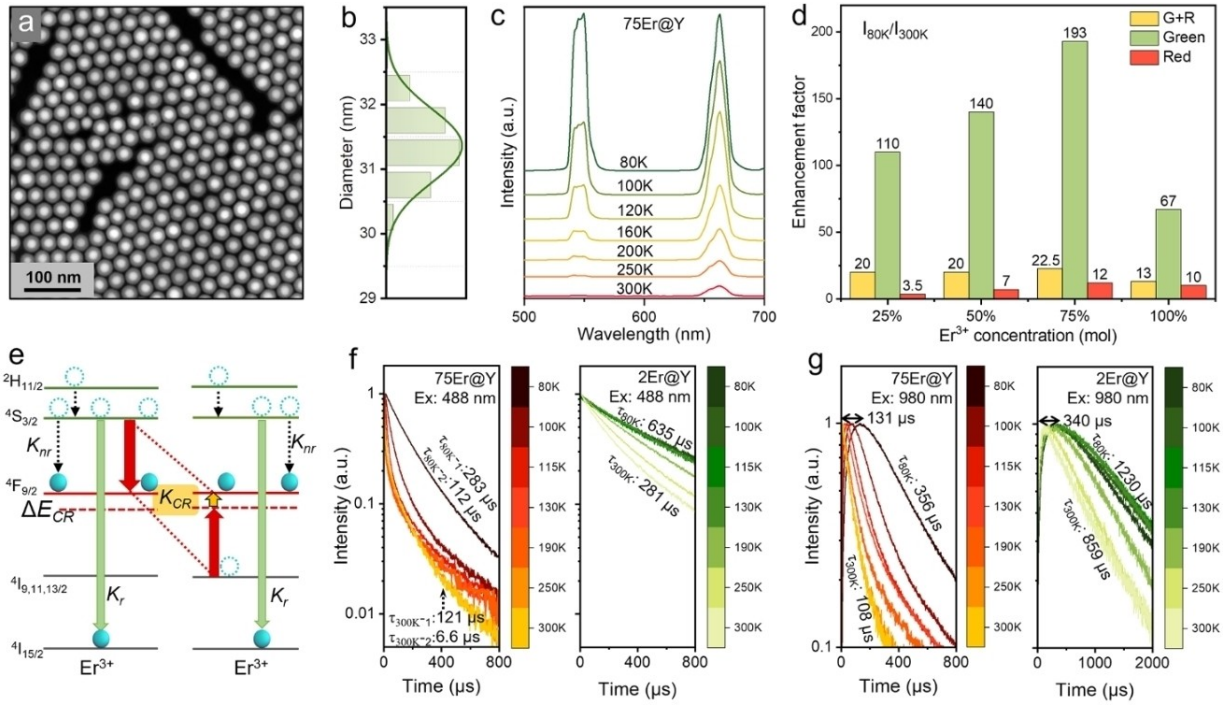

Figure 2. a) The high-angle annular dark field (HAADF) TEM image, and b) The statistical size distribution, of the synthesized $NaErF_4$@$NaYF_4$ nanoparticle. c) Temperature-dependent UC emission spectra of $NaYF_4$:75 %Er^{3+}@$NaYF_4$ nanosystem (taking as an example), under 10 W/cm^2 980 nm excitation. d) The low-temperature induced UC enhancement factor (i.e., I_{80K}/I_{300K}) of series Er^{3+}-rich nanostructures, in which the Er^{3+} concentration varies from 25 % to 100 %. e) The simplified depopulation processes in Er^{3+}-rich nanosystem, including radiative emission (K_r), non-radiative transition (K_{nr}), and temperature-related CR (K_{CR}). f) The temperature dependent 545 nm emission decay curves of high-doped $NaYF_4$:75 %Er^{3+}@$NaYF_4$ (left) and low-doped $NaYF_4$:2 %Er^{3+}@$NaYF_4$ (right) under 488 nm pulsed excitation, g) The temperature dependent 545 nm emission decay curves of high-doped $NaYF_4$:75 %Er^{3+}@$NaYF_4$ (left) and low-doped $NaYF_4$:2 %Er^{3+}@$NaYF_4$ (right) under 980 nm pulsed excitation.

Besides, the optimal Er^{3+} concentration in the core is confirmed to be 75 %, above which, low temperature-induced UC enhancement starts to fade (Figure 2d), indicating the strong interaction between the Er^{3+} and 80 K is insufficient to effectively suppress the CR.

Apparently, the dramatic enhancement of PL induced by cryogenic cooling provides a new opportunity to break the bottleneck of UC efficiency. However, further developments and applications strongly rely on in-depth and comprehensive studies of the enhancement mechanism, where a quantitative description is an essential precondition. First of all, we start with a simplified model where only one CR channel is considered (Figure 2e). In that case, the $^4S_{3/2}$ level of Er^{3+} has three depopulation channels, i.e., radiative transition (with rate K_r), non-radiative relaxation (with rate K_{nr}), and CR relaxation (with rate K_{CR}). The UC intensity of green emission (i.e., I_g) is thus:

$$I_g = N[K_r/(K_r + K_{nr} + K_{CR})] \quad (1)$$

where N is the population on $^4S_{3/2}$ level.

Notably, only in the case of high doping, the depopulation process can be dominated by CR, i.e., $k_{CR} \gg k_r$, k_{nr}, because the ion-to-ion interaction distance in high doping system is very short and the CR rate is thus very high. This assumption is further experimentally validated by the 545 nm down-shifting decay dynamics (excited by nanosecond 488 nm pulse). As shown in Figure 2f, the control group (i.e., the low-doped $NaYF_4$:2 %Er^{3+}@$NaYF_4$ structure, 2Er@Y for short) consistently exhibits a relatively long decay lifetime (281–635 μs) over a wide temperature range (80–300 K), while an ultra-fast decay process (~6.6 μs) is clearly observed for the 75Er@Y high doping structure when the temperature is 300 K. This difference unambiguously indicates the existence of efficient CR in 75Er@Y structure (if $T > 100$ K, more detailed results are shown in Figure S7 and Table S1–2), whose strength is significantly larger than the K_r and K_{nr}. Notably, such ultra-fast decay cannot be observed if we tune the pulse excitation to 980 nm (Figure 2g). Instead of that, a significantly prolonged rise time appears (with temperature decreasing). All these differences can be well attributed to the natural character of the UC (i.e., excitation at 980 nm and emission at 545 nm), in which the influence of the intermediate energy level (e.g., $^4I_{11/2}$) on PL dynamics cannot be ignored. Specifically, with temperature decreasing, the prolonged energy transfer/migration processes on intermediate energy level expand both the rise and decay time of the UC PL (Figure 2g, the fitting details are shown in Figure S7 and Table S3–4).[6e] Consequently, the intrinsic ultra-fast decay from the UC emitting energy level will be covered by the expanded signals. Furthermore, according to the previous reports,[15]

the rate of phonon-assisted energy transfer process (including CR) can be described as follows:

$$K_{CR} \propto A\ exp(-\Delta E_{CR}/k_B T) \tag{2}$$

where A is a constant, k_B is the Boltzmann constant, and T is the absolute temperature. Therefore, taking the dominated role of CR into consideration (i.e., $k_{CR} \gg k_r$, k_{nr}), for the Er^{3+}-rich UC system, Eq. 1 can be rewritten as:

$$I_g \propto A_1\ exp(\Delta E_{CR}/k_B T) \tag{3}$$

where A_1 is a constant. Notably, for the first time, Eq. 3 provides a fundamental understanding to the extremely strong temperature-to-PL response (over two orders of magnitude) of Er^{3+}-rich UCNPs.

Next, more complex CR channels are considered to fit the real situation. As shown in Figure 3a, because of the nearly perfect ladder-like energy levels of Er^{3+}, numerous CR channels are potentially allowed in this UC system. Obviously, sorting out each role of them remains a challenge. However, based on their working effects on temperature response, these channels can be roughly classified into two types: (1) CR1 with relatively small ΔE (100–250 cm^{-1}), and (2) CR2 with relatively large ΔE (600–900 cm^{-1}). Accordingly, Eq. 3 should be modified as:

$$1/I_g \propto (K_{CR1} + K_{CR2}) = B_{CR1}(-\Delta E_1/k_B T) + B_{CR2}\ (-\Delta E_2/k_B T) \tag{4}$$

where $B_{CR1,2}$ are constants, $\Delta E_{1,2}$ are the energy gap mismatches of two CR channels. From Eq. 4, it is important to realize that the variation of I_g relies on the collective effects of ΔE_1 and ΔE_2, which provides a new and convenient method to tune the temperature response of UCNPs by simply changing the excitation power density (ρ_{ex}). As discussed in the Supporting Information (see the calculation part), the low-temperature induced UC enhancement factor (i.e., I_{80k}/I_{300k}) significantly decreases with decreasing ΔE. Therefore, if the proportion of CR1 (with a smaller energy gap) in the overall CR channels can be simultaneously increased with ρ_{ex}, a gradually decreased factor (I_{80k}/I_{300k}) will be expected, which is indeed observed from our experimental results. As shown in Figure 3b and Figure S8, with ρ_{ex} increasing from 6 to 50 W/cm^2, the factor I_{80k}/I_{300k} significantly declines from 268 to 75. This phenomenon can be partly attributed to the faster growth (with increased ρ_{ex}) of the excited states' population of $^4I_{9/2}$ (involved to CR1 channel) than other competitors (i.e., populations on $^4I_{11/2}$, $^4I_{13/2}$) As shown in Figure S9 (the excitation power dependent emission spectra), the population of $^4I_{9/2}$ grows nonlinearly with the increased ρ_{ex}, while the competitors show strictly linear growth. Therefore, the increased ρ_{ex} promotes

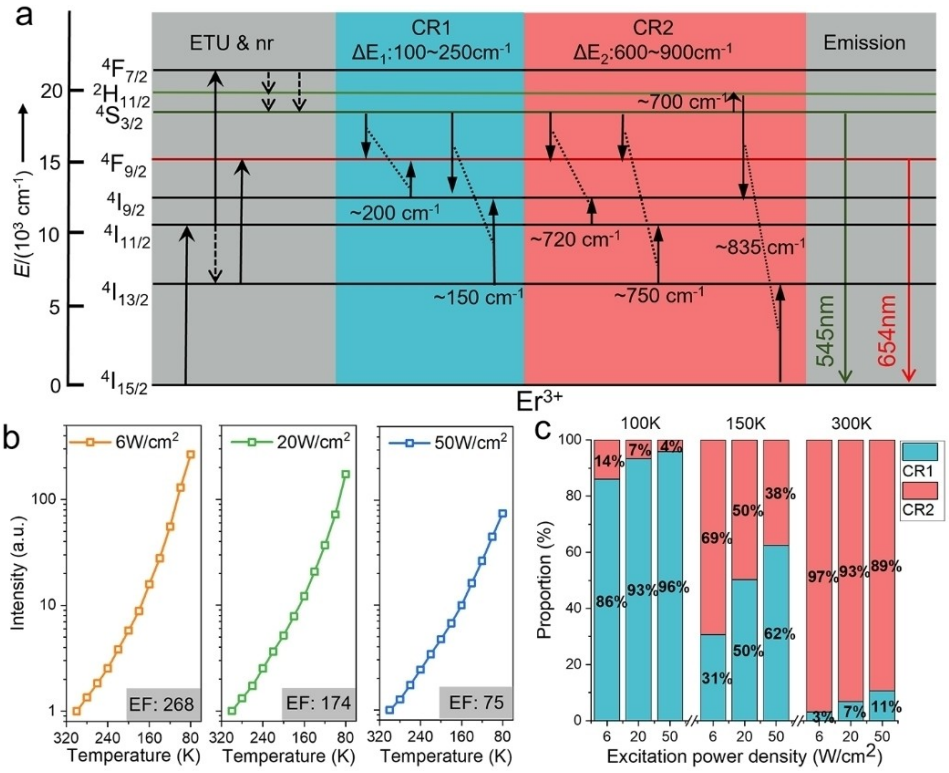

Figure 3. a) The potential CR channels for the green UC emission of Er^{3+}-rich nanosystems. All channels can be classified into two types (i.e., CR1 and CR2), according to the required energy gap in CR. b) The measured temperature dependent (from 300 to 80 K) green UC emission intensity of 75Er@Y nanostructure, the 980 nm excitation densities are 6, 20, and 50 W/cm^2, respectively. c) The fitted proportion of two CR channels in 75Er@Y nanostructure.

the contribution of CR1 channel. Furthermore, according to Eq. 4, the contribution of these two CR channels (i.e., the proportion of K_{CR1} and K_{CR2}) can also be quantitatively obtained from the dual-exponential fitting of the I_g-T curves in Figure 3b (the ΔE_1 and ΔE_2 are set as 200 cm^{-1} and 750 cm^{-1}, respectively). Fitting results are shown in Figure 3c, and two points can be found: (1) as expected, the contribution of the CR1 channel indeed increases with ρ_{ex}, and (2) the working CR channel is also controlled by temperature. Specifically, at relatively low temperatures (e.g., 80–150 K), due to the limited phonon energy, only the CR1 channel (with the smaller ΔE) can be efficiently activated. On the contrary, the CR2 channel will gradually play a major role from 150 to 300 K (detailed fitting results are shown in Figure S10 and Table S5–6).

Based on the temperature hypersensitivity of the UC emission of Er^{3+}-rich nanostructures, one natural application is to construct an ultra-sensitive remote temperature sensor. As shown in Figure 4a, most conventional rare-earth based sensors rely on the thermal coupling of two closely lying energy levels within the same configuration.[16] The luminescence intensity ratio (LIR) of these two energy levels follows a simple Boltzmann law (i.e., Eq. 5):

$$LIR = I_{up}/I_{low} = C\ exp(-\Delta E_{21}/k_B T) \quad (5)$$

where I_{up} and I_{low} are the emission intensities of two thermally coupled levels, C is a fitting constant, and ΔE_{21} is the energy gap between these two energy levels. The flaw of this strategy is that the choice of suitable thermally coupled

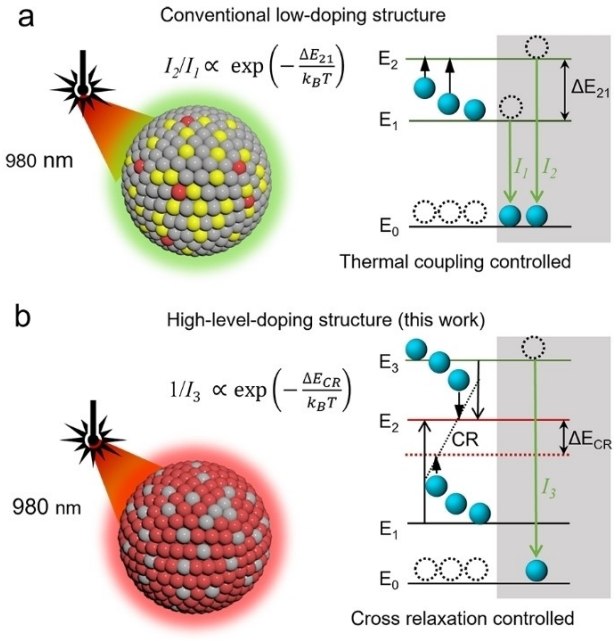

Figure 4. Schematic illustration of upconversion thermal response in two different doping strategies. a) In the conventional low-doping system, e.g., 20Yb2Er@Y, the populations on two thermal couple energy levels are controlled by Boltzmann law. b) In the high-level-doping system, e.g., Er^{3+}-rich core–shell system, the PL intensity has an exponential relation with temperature.

energy levels is very limited, which is usually not conducive to obtaining satisfactory temperature sensitivity at relatively low temperatures (e.g., below 150 K).[17] This dilemma, however, can be solved to some extent by introducing a new working mechanism, i.e., the CR strength controlled UC intensity. As shown in Figure 4b, if we monitor the PL intensity of a CR dominated high doping system, the role of ΔE_{21} (in conventional systems) can be replaced by ΔE_{CR}. Especially, due to the relatively small value of ΔE_{CR1} (100–250 cm^{-1}, much less than most of the alternative energy gaps in traditional thermal coupling strategy), the sensing range of Er^{3+}-rich nanostructure is expected to be greatly shifted to the lower temperature.

To examine our assumption, a core/multi-shell structure is constructed, i.e., $NaYF_4$:75 %Er^{3+}@$NaYF_4$@$NaYF_4$:75 % Yb^{3+}, 2 %Tm^{3+}@$NaYF_4$ (labeled as C-S1-S2-S3, Figure 5a). The sizes of the core and multi-shells are demonstrated to 12, 7, 5.5, and 9 nm, respectively (Figure 5b). Besides, the elements' distributions in the UCNPs are solidly confirmed by HAADF-STEM (high-angle annular dark-field scanning transmission electron microscopy), EELS (electron energy loss spectroscopy), and EDS-mapping (energy-dispersive X-ray spectroscopy mapping), which are well in line with our design (Figure 5b, c).

Rest characterizations are provided in Figures S11–14. The purpose of adding Yb^{3+}/Tm^{3+} components is to provide a temperature-insensitive reference signal at 475 nm (more details are discussed in Figure S15–18, including the optimization of the doping concentrations of Yb^{3+} and Tm^{3+}). Subsequently, the temperature-dependent UC spectra of this core/multi-shell structure are displayed in Figure 5d–f and Figure S14 (excited by 10 W/cm^2 980 nm laser). Specifically, the 545 nm emission from Er^{3+} in the core shows a remarkable enhancement (173-fold) with temperature decreasing from 300 to 80 K. On the contrary, the variation of 475 nm emission from Tm^{3+} in the S2 shell is limited to 3-fold. Therefore, the I_{475nm}/I_{545nm} emission ratio can be used for temperature sensing (Figure 5g). In a wide range (80–300 K), this ratio can be divided into two regions, i.e. above and below 150 K, and an exponential relationship maintains in each of the two regions. The turning point of 150 K is distinct in Figure 5g (notably, the boundary temperature 150 K exhibits a good fit for both curves). Furthermore, the indexes of absolute and relative sensitivity (S_a and S_r), which are essential for assessing the optical thermometry property, can be calculated by:

$$S_a = dR/dT;\ S_r = dR/(R^* dT) \quad (6)$$

As shown in Figure 5h, the as-designed core/multi-shell structure exhibits an extremely sensitive response in cryogenic field due to the small ΔE value of CR1. The maximum calculated values of S_a and S_r reach 11.7 % (at 150 K) and 12.3 % (at 80 K), respectively. Additionally, the superior stability and repeatability of the sensor are assured in Figure 5i, in which the results of eight cycles between 80 and 300 K are displayed. It is worth noting that compared with the popular low-doping strategies (relevant results are labeled in Table S7) our design bases on a completely

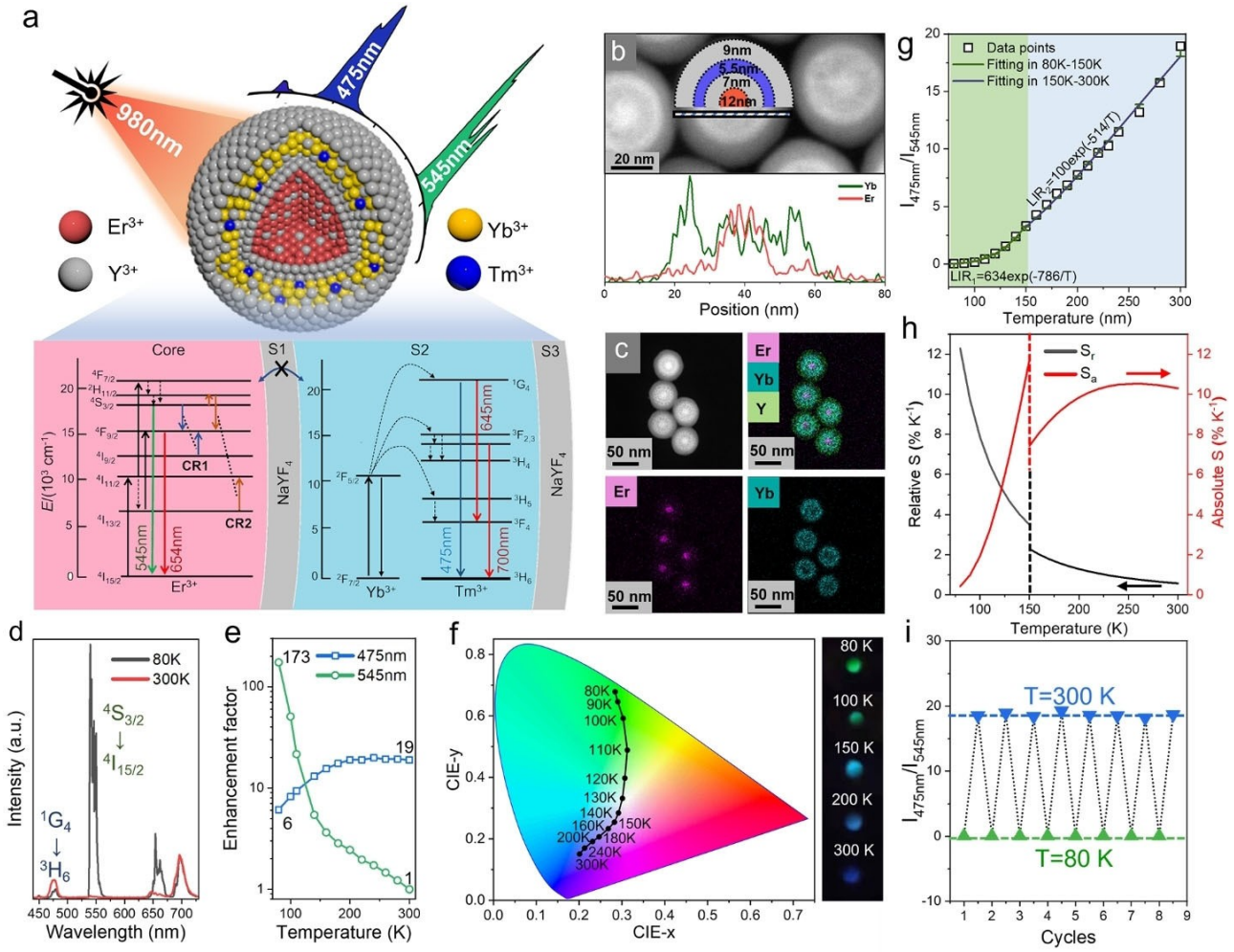

Figure 5. a) The luminescence processes in core/multi-shell UCNPs. b) The magnified HAADF-STEM image (up) and the electron energy loss spectroscopy (EELS) analysis (down) of the UCNPs. c) EDS-mapping image results of five selected UCNPs. d) UC emission spectra of core/multi-shell UCNPs at 80 and 300 K, respectively (Ex: 980 nm, 6 W/cm^2). e) The temperature dependent 475 nm and 545 nm emission intensities of core/multi-shell UCNPs (from 300 to 80 K). f) CIE chromaticity diagram of emission colors for the core/multi-shell UCNPs at various temperatures. The beside photographs show the emission colors of UCNPs powder under different temperatures. g) LIR and corresponding fitted curves of core/multi-shell UCNPs. h) Relative and absolute sensitivity of core/multi-shell UCNPs. i) Repeatability test of emission intensity ratio (I_{475nm}/I_{545nm}) recorded at 80 K and 300 K over eight cycles.

different new mechanism (i.e., CR manipulated UC intensity), which owns two unique advantages: (1) the temperature variation of the environment can be intuitively estimated from the output color (as shown in Figure 5f and the photos beside), while the traditional design usually has to rely on the professional instrument measurement (e.g., the emission ratio of 525 nm/545 nm). Therefore, our design facilitates a quick evaluation. (2) Benefiting from the extremely efficient temperature response of the Er^{3+}-rich part, in the cryogenic range (80–150 K), our design has an over 10-fold higher sensitivity, while conventional strategies are restricted by the weak thermal population, and fail to execute effective measurements in this temperature range (Figure S19–20). Based on these unique advantages, we believe our designed UCNPs hold significant potential for diverse applications, including low-temperature imaging, anti-counterfeiting, precisely monitoring the temperature of spacecraft and some precision instruments.

Conclusion

In summary, the working mechanism underlying the over 100-fold enhancement of green UC emission of Er^{3+}-rich nanophosphors at cryogenic temperature was quantitatively unraveled. The exponential relation between green UC intensity and the environmental temperature was well documented from theory and experiments for the first time. Furthermore, the super-sensitivity temperature response of the UC emission can be attributed to the joint effect of two types of CR channels (separated by different energy gap values). As proof of the principle of application, we have proposed and validated a novel strategy of temperature

sensing utilizing Er^{3+}-rich nanostructures. Benefitting from the new working mechanism (CR manipulated UC intensity) in our design structure, it provides an over 10-fold higher sensitivity in the low-temperature range.

Acknowledgements

This research was supported by the National Natural Science Foundation of China (Grants 12104179, 11874055, 62075217, 62075215, 22172154), the Jilin Provincial Department of Science and Technology (Grants 20210101148JC, 20230508104RC, and 202512JC010475440), NWO TTW perspective project MEDPHOT, EU H2020MSCA-RISE-2017 Action program, CANCER, under grant nr. 777682.

Conflict of Interest

The authors declare no conflict of interest.

Data Availability Statement

The data that support the findings of this study are available from the corresponding author upon reasonable request.

Keywords: Upconversion Nanoparticle · Er^{3+}-Rich Nanophosphor · Cross Relaxation · Excitation Power Tailor · Temperature Sensing

[1] a) S. Han, R. Deng, X. Xie, X. Liu, *Angew. Chem. Int. Ed.* **2014**, *53*, 11702–11715; b) M. Haase, H. Schäfer, *Angew. Chem. Int. Ed.* **2011**, *50*, 5808–5829; c) F. Auzel, *Chem. Rev.* **2004**, *104*, 139–174.

[2] a) L. Cheng, K. Yang, Y. Li, J. Chen, C. Wang, M. Shao, S.-T. Lee, Z. Liu, *Angew. Chem. Int. Ed.* **2011**, *50*, 7385–7390; b) O. S. Wolfbeis, *Chem. Soc. Rev.* **2015**, *44*, 4743–4768; c) P. Pei, Y. Chen, C. Sun, Y. Fan, Y. Yang, X. Liu, L. Lu, M. Zhao, H. Zhang, D. Zhao, X. Liu, F. Zhang, *Nat. Nanotechnol.* **2021**, *16*, 1011–1018; d) D. B. L. Teh, A. Bansal, C. Chai, T. B. Toh, R. A. J. Tucker, G. G. L. Gammad, Y. Yeo, Z. Lei, X. Zheng, F. Yang, J. S. Ho, N. Bolem, B. C. Wu, M. K. Gnanasammandhan, L. Hooi, G. S. Dawe, C. Libedinsky, W. Ong, B. Halliwell, E. K. Chow, K. Lim, Y. Zhang, B. K. Kennedy, *Adv. Mater.* **2020**, *32*, 2001459; e) J.-C. Zhou, Z.-L. Yang, W. Dong, R.-J. Tang, L.-D. Sun, C.-H. Yan, *Biomaterials* **2011**, *32*, 9059–9067; f) Y. Feng, Y. Wu, J. Zuo, L. Tu, I. Que, Y. Chang, L. J. Cruz, A. Chan, H. Zhang, *Biomaterials* **2019**, *201*, 33–41.

[3] a) M. You, J. Zhong, Y. Hong, Z. Duan, M. Lin, F. Xu, *Nanoscale* **2015**, *7*, 4423–4431; b) R. Huang, S. Liu, J. Huang, H. Liu, Z. Hu, L. Tao, B. Zhou, *Nanoscale* **2021**, *13*, 4812–4820; c) X. Liu, Y. Wang, X. Li, Z. Yi, R. Deng, L. Liang, X. Xie, D. T. B. Loong, S. Song, D. Fan, A. H. All, H. Zhang, L. Huang, X. Liu, *Nat. Commun.* **2017**, *8*, 899.

[4] a) Y. Liu, Y. Lu, X. Yang, X. Zheng, S. Wen, F. Wang, X. Vidal, J. Zhao, D. Liu, Z. Zhou, C. Ma, J. Zhou, J. A. Piper, P. Xi, D. Jin, *Nature* **2017**, *543*, 229–233; b) Q. Zhan, H. Liu, B. Wang, Q. Wu, R. Pu, C. Zhou, B. Huang, X. Peng, H. Ågren, S. He, *Nat. Commun.* **2017**, *8*, 1058; c) Y. Shang, J. Zhou, Y. Cai, F. Wang, A. Fernandez-Bravo, C. Yang, L. Jiang, D. Jin, *Nat. Commun.* **2020**, *11*, 6156.

[5] a) K. R. Mun, J. Kyhm, J. Y. Lee, S. Shin, Y. Zhu, G. Kang, D. Kim, R. Deng, H. S. Jang, *Nano Lett.* **2023**, *23*, 3014–3022; b) L. Gao, X. Shan, X. Xu, Y. Liu, B. Liu, S. Li, S. Wen, C. Ma, D. Jin, F. Wang, *Nanoscale* **2020**, *12*, 18595–18599; c) R. Deng, F. Qin, R. Chen, W. Huang, M. Hong, X. Liu, *Nat. Nanotechnol.* **2015**, *10*, 237–242.

[6] a) F. Wang, R. Deng, J. Wang, Q. Wang, Y. Han, H. Zhu, X. Chen, X. Liu, *Nat. Mater.* **2011**, *10*, 968–973; b) C. Homann, L. Krukewitt, F. Frenzel, B. Grauel, C. Würth, U. Resch-Genger, M. Haase, *Angew. Chem. Int. Ed.* **2018**, *57*, 8765–8769; c) Y. Zhong, G. Tian, Z. Gu, Y. Yang, L. Gu, Y. Zhao, Y. Ma, J. Yao, *Adv. Mater.* **2014**, *26*, 2831–2837; d) B. Zhou, L. Yan, J. Huang, X. Liu, L. Tao, Q. Zhang, *Nat. Photonics* **2020**, *14*, 760–766; e) J. Zuo, D. Sun, L. Tu, Y. Wu, Y. Cao, B. Xue, Y. Zhang, Y. Chang, X. Liu, X. Kong, W. J. Buma, E. J. Meijer, H. Zhang, *Angew. Chem. Int. Ed.* **2018**, *57*, 3054–3058.

[7] a) B. Chen, F. Wang, *Acc. Chem. Res.* **2020**, *53*, 358–367; b) S. Wen, J. Zhou, K. Zheng, A. Bednarkiewicz, X. Liu, D. Jin, *Nat. Commun.* **2018**, *9*, 2415.

[8] a) G. Chen, J. Damasco, H. Qiu, W. Shao, T. Y. Ohulchanskyy, R. R. Valiev, X. Wu, G. Han, Y. Wang, C. Yang, H. Ågren, P. N. Prasad, *Nano Lett.* **2015**, *15*, 7400–7407; b) X. Li, R. Wang, F. Zhang, D. Zhao, *Nano Lett.* **2014**, *14*, 3634–3639; c) J. Zhao, D. Jin, E. P. Schartner, Y. Lu, Y. Liu, A. V. Zvyagin, L. Zhang, J. M. Dawes, P. Xi, J. A. Piper, E. M. Goldys, T. M. Monro, *Nat. Nanotechnol.* **2013**, *8*, 729–734.

[9] a) Q. Chen, X. Xie, B. Huang, L. Liang, S. Han, Z. Yi, Y. Wang, Y. Li, D. Fan, L. Huang, X. Liu, *Angew. Chem. Int. Ed.* **2017**, *56*, 7605–7609; b) J. Zuo, Q. Li, B. Xue, C. Li, Y. Chang, Y. Zhang, X. Liu, L. Tu, H. Zhang, X. Kong, *Nanoscale* **2017**, *9*, 7941–7946; c) N. J. J. Johnson, S. He, S. Diao, E. M. Chan, H. Dai, A. Almutairi, *J. Am. Chem. Soc.* **2017**, *139*, 3275–3282.

[10] a) X. Cheng, Y. Pan, Z. Yuan, X. Wang, W. Su, L. Yin, X. Xie, L. Huang, *Adv. Funct. Mater.* **2018**, *28*, 1800208; b) L. Liu, S. Wang, B. Zhao, P. Pei, Y. Fan, X. Li, F. Zhang, *Angew. Chem. Int. Ed.* **2018**, *57*, 7518–7522; c) L. Yan, B. Zhou, N. Song, X. Liu, J. Huang, T. Wang, L. Tao, Q. Zhang, *Nanoscale* **2018**, *10*, 17949–17957.

[11] a) J. Zuo, L. Tu, Q. Li, Y. Feng, I. Que, Y. Zhang, X. Liu, B. Xue, L. J. Cruz, Y. Chang, H. Zhang, X. Kong, *ACS Nano* **2018**, *12*, 3217–3225; b) Y. Feng, X. Liu, Q. Li, S. Mei, K. Wu, J. Yuan, L. Tu, I. Que, F. Tamburini, F. Baldazzi, A. Chan, L. J. Cruz, J. Zuo, C. Yao, H. Zhang, *J. Mater. Chem. C* **2022**, *10*, 688–695; c) H. Wang, W. Lu, T. Zeng, Z. Yi, L. Rao, H. Liu, S. Zeng, *Nanoscale* **2014**, *6*, 2855–2860.

[12] a) T. Sun, Y. Li, W. L. Ho, Q. Zhu, X. Chen, L. Jin, H. Zhu, B. Huang, J. Lin, B. E. Little, S. T. Chu, F. Wang, *Nat. Commun.* **2019**, *10*, 1811; b) Q. Li, X. Li, L. Zhang, J. Zuo, Y. Zhang, X. Liu, L. Tu, B. Xue, Y. Chang, X. Kong, *Nanoscale* **2018**, *10*, 12356–12363; c) F. Ren, H. Liu, H. Zhang, Z. Jiang, B. Xia, C. Genevois, T. He, M. Allix, Q. Sun, Z. Li, M. Gao, *Nano Today* **2020**, *34*, 100905; d) Y. Li, Y. Li, Y. Bai, R. Wang, L. Lin, Y. Sun, *RSC Adv.* **2020**, *10*, 38416–38423.

[13] L. Tu, K. Wu, Y. Luo, E. Wang, J. Yuan, J. Zuo, D. Zhou, B. Li, J. Zhou, D. Jin, H. Zhang, *Angew. Chem. Int. Ed.* **2023**, *62*, e202217100.

[14] a) W. Wei, Y. Zhang, R. Chen, J. Goggi, N. Ren, L. Huang, K. K. Bhakoo, H. Sun, T. T. Y. Tan, *Chem. Mater.* **2014**, *26*, 5183–5186; b) C. Lee, H. Park, W. Kim, S. Park, *Phys. Chem. Chem. Phys.* **2019**, *21*, 24026–24033.

[15] a) T. Miyakawa, D. L. Dexter, *Phys. Rev. B* **1970**, *1*, 2961–2969; b) X. Zhu, X. Wang, H. Zhang, F. Zhang, *Angew. Chem. Int. Ed.* **2022**, *61*, e202209378.

[16] a) F. Vetrone, R. Naccache, A. Zamarrón, A. Juarranz de la Fuente, F. Sanz-Rodríguez, L. Martinez Maestro, E.

Martín Rodriguez, D. Jaque, J. García Solé, J. A. Capobianco, *ACS Nano* **2010**, *4*, 3254–3258; b) D. Yu, H. Li, D. Zhang, Q. Zhang, A. Meijerink, M. Suta, *Light-Sci. Appl.* **2021**, *10*, 236; c) T. P. van Swieten, J. M. Steenhoff, A. Vlasblom, R. de Berg, S. P. Mattern, F. T. Rabouw, M. Suta, A. Meijerink, *Light-Sci. Appl.* **2022**, *11*, 343; d) X. Wang, Y. Wang, J. Marques-Hueso, X. Yan, *Sci. Rep.* **2017**, *7*, 758; e) M. K. Mahata, T. Koppe, K. Kumar, H. Hofsäss, U. Vetter, *Sci. Rep.* **2020**, *10*, 8775.

[17] a) L. T. K. Giang, K. Trejgis, L. Marciniak, N. Vu, L. Q. Minh, *Sci. Rep.* **2020**, *10*, 14672; b) S. Sinha, M. K. Mahata, K. Kumar, S. P. Tiwari, V. K. Rai, *Spectrochim. Acta Part A* **2017**, *173*, 369–375; c) G. Xiang, Q. Xia, X. Liu, X. Wang, *Dalton Trans.* **2020**, *49*, 17115–17120; d) Q. Qiang, S. Du, X. Ma, W. Chen, G. Zhang, Y. Wang, *Dalton Trans.* **2018**, *47*, 8656–8662.

Manuscript received: May 10, 2023
Accepted manuscript online: June 22, 2023
Version of record online: June 22, 2023